Current Opinion in Solid State and Materials Science 44 (2026) 101273

Contents lists available at ScienceDirect

Current Opinion in Solid State & Materials Science

journal homepage: www.elsevier.com/locate/cossms

Bimodal piezotronic tactile sensor for Morse code recognition using patterned ZnO nanoarrays

Weili Deng [a,*], Zihan Wang [a], Hongguang Li [a], Peiwen Li [a], Jinlong Sun [a], Zhiyuan Gao [a], Shenglong Wang [a], Long Jin [a], Weiqing Yang [a,b]

[a] Key Laboratory of Advanced Technologies of Materials (Ministry of Education), School of Materials Science and Engineering, Southwest Jiaotong University, Chengdu 610031, PR China

[b] Research Institute of Frontier Science, Southwest Jiaotong University, Chengdu 610031, PR China

ARTICLE INFO

Keywords:
Piezotronic sensor
Patterned ZnO nanorods
Tactile recognition
Bimodal detection
Piezoelectric screening effect

ABSTRACT

Tactile sensing is pivotal for precise environmental interaction in robotics, smart manufacturing, and intelligent healthcare. However, conventional force sensors frequently struggle to reconcile sensitivity and linearity with biomimetic multifunctionality, particularly the dual-mode (static/dynamic) sensing capability of human skin. To bridge this gap, we propose a bimodal piezotronic tactile sensor utilizing patterned ZnO nanorod arrays. Both the simulation and experimental results confirm that the patterned architecture effectively suppresses the piezoelectric screening effect, yielding a twofold enhancement in piezoelectric output compared to continuous film counterparts. Crucially, the developed device overcomes the inherent limitations of conventional piezoelectric sensors regarding static stimuli, achieving stable static force sensing for over 1000 s while maintaining a decent dynamic responsiveness. As a proof-of-concept, the sensor is integrated with a deep learning algorithm to decode Morse code, demonstrating a recognition accuracy of 99%. This work enriches the theoretical framework for designing high-performance bimodal piezotronic devices, offering new strategies for advanced wearable electronics and seamless human–machine interactions.

1. Introduction

Tactile sensing is essential to biological systems, facilitating mechanical stimuli perception and governing body awareness and environmental interactions [1–3]. This ability to precisely discern spatial location, object morphology, and applied pressure is critical for advancing robotics, healthcare, and artificial intelligence [4–6]. Consequently, the development of advanced tactile sensors capable of transducing mechanical stimuli into stable electrical signals has emerged as a central research focus [7,8]. Although considerable progress has been achieved using capacitive, piezoresistive, or triboelectric mechanisms [9–13], intrinsic constraints hinder their efficacy in bimodal (static/dynamic) detection. Specifically, triboelectric sensors are fundamentally incapable of detecting static pressure, while piezoresistive and capacitive sensors often suffer from inadequate high-frequency dynamic response due to material relaxation and response time constraints. To overcome these limitations, hybrid architectures integrating two or more mechanisms (e.g., piezoelectric-triboelectric, triboelectric-piezoresistive, and capacitive-triboelectric combinations) have been widely explored [14–16]. Although such approaches can realize dual-mode functionality, they typically rely on stacking distinct functional layers, introducing challenges such as complex signal decoupling, increased device thickness, elevated fabrication costs, and structural heterogeneity, which can impede practical integration and application [17,18]. Therefore, a monolithic sensing strategy capable of high-sensitivity, bimodal detection within a simplified structural framework is highly desirable.

The emergence of piezotronics offers a promising alternative by leveraging piezoelectric polarization charges to directly modulate interfacial barrier heights and carrier transport [19–24]. This effect is particularly prominent in wurtzite-structure semiconductors (such as ZnO, GaN, CdS, etc.), where piezoelectric and semiconducting properties are inherently coupled [25–28]. In piezotronic devices, the piezoelectric potential functions as a “gate” signal, enabling exponential modulation of the output current and thereby offering intrinsically high sensitivity for mechanical sensing [29–34]. This principle represents a

* Corresponding author.
E-mail address: weili1812@swjtu.edu.cn (W. Deng).

https://doi.org/10.1016/j.cossms.2026.101273
Received 29 January 2026; Received in revised form 3 April 2026; Accepted 3 May 2026
Available online 6 May 2026
1359-0286/© 2026 Elsevier Ltd. All rights are reserved, including those for text and data mining, AI training, and similar technologies.

distinct control mechanism, differing fundamentally from traditional CMOS technology in its design and application [35,36]. Among the numerous piezotronic materials, ZnO is particularly attractive due to its facile synthesis, biosafety and low cost [37–39]. To enhance device efficiency, several strategies aimed at boosting piezoelectricity or mitigating the screening effect of free carriers on piezoelectric polarization charges have been developed, including doping, alloying, patterning, surface treatment, and interfacial modification [40–43]. Typical material modification approaches seek to optimize performance by altering the internal properties of the material, for instance, by introducing lattice defects and distortions through doping, or by generating holes via hydrogen annealing treatment to deplete carriers [44]. From a structural perspective, vertically aligned ZnO nanowire devices maximize the utilization of polarization charges along the c-axis, while dual-channel configurations enhance operational stability [45]. To date, research has predominantly focused on dynamic force monitoring or coupling piezoelectric properties with photoelectric performance to expand multifunctional application scenarios [46–48]. However, the development of integrated sensing systems for both dynamic and static forces remains largely nascent. This gap significantly limits the adaptability of ZnO-based piezotronic devices in complex practical sensing environments [49–51].

In this work, we report a bimodal piezotronic device (PZBD) based on patterned ZnO nanorod arrays, fabricated via low-temperature hydrothermal synthesis and photolithography. The spatially discrete architecture effectively suppresses the piezoelectric screening effect, substantially enhancing piezotronic performance. Through theoretical simulation and experimental characterization, the underlying mechanism for this enhancement is elucidated from carrier concentration modulation and interfacial polarization charge distribution. Leveraging the optimized piezotronic effect, the PZBD achieves robust bimodal sensing for both dynamic stimuli and static forces. As a proof-of-concept demonstration, we integrate the sensor with a deep learning algorithm to implement accurate Morse code recognition, showcasing its unique bimodal perception capabilities. This work offers a viable approach for constructing bimodal tactile sensors, opening new avenues for intelligent human–machine interaction systems.

2. Results and discussion

2.1. Working mechanism of PZBD

The performance of piezotronic devices is fundamentally governed by the modulation of the Schottky barrier via strain-induced polarization charges. Therefore, enhancing the inherent piezoelectricity of semiconductors is a common approach for constructing high-performance piezotronic sensors. A primary limitation of ZnO-based devices is the piezoelectric screening effect, where the redistributed free carriers neutralize the strain-induced polarization charges and attenuate the effective piezopotential. To mitigate this fundamental issue, we fabricated patterned ZnO nanorod (NR) arrays via photolithography. As illustrated in Fig. 1**a**, the microstructure consists of discrete, independent arrays, which effectively reduces the effective volume for bulk carrier transport and suppresses lateral leakage pathways. To better understand this screening effect, Fig. 1**b** depicts the carrier state within a continuous ZnO film, where the facile movement of free electrons significantly weakens the piezopotential under mechanical stress. In contrast, the patterned architecture promotes carrier depletion due to its increased surface-to-volume ratio and confined geometry, thereby mitigating the screening effect (Fig. 1**c**). This structural

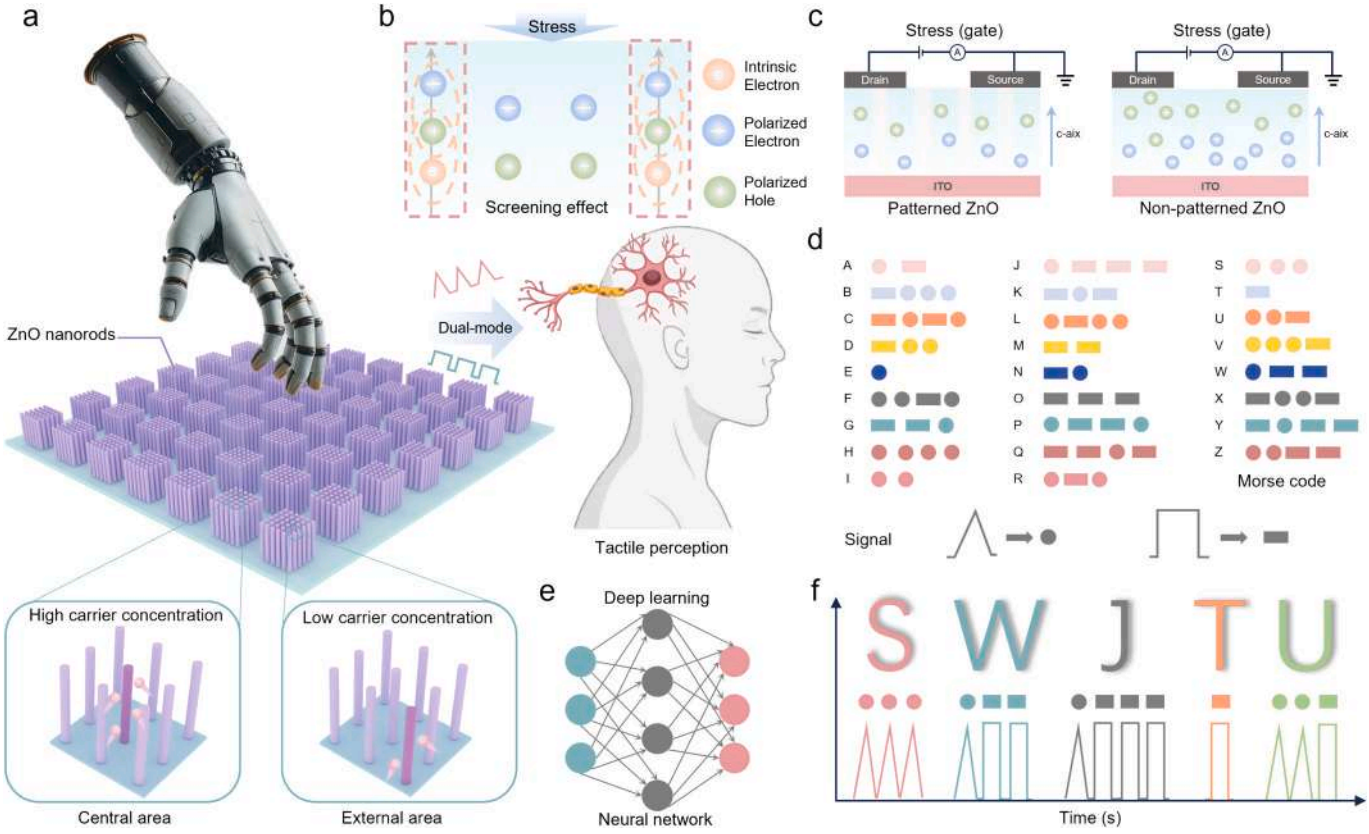


Fig. 1. Conception and design of PZBD. (a) Application scenario of PZBD. (b) Schematic diagram of the piezoelectric screening effect. (c) Comparison of the sensing performance between patterned and non-patterned ZnO. (d) Electrical signal features are mapped to letters via the Morse code-based correspondence. (e) Deep learning networks convert electrical signals into brain-like neural signals. (f) Tactile signals captured by the sensor are decoded into characters, completing the closed loop from tactile perception to information encoding.

optimization allows a higher density of polarization charges to be retained at the interface. The resulting robust modulation of the interfacial barrier significantly enhances the responsiveness of the device. By utilizing this improved electromechanical coupling for both static and dynamic sensing, we integrated the PZBD into a Morse code translation system (Fig. 1**d**). The PZBD possesses the unique capability to distinguish between transient (dynamic) and sustained (static) mechanical inputs. This enables the encoding of the 26 English letters as distinct combinations of these dynamic and static signals. As a proof of concept, we coupled the sensor with a deep learning algorithm for signal classification (Fig. 1**e**). The system successfully decoded a sequence of mechanical inputs into the alphabetic letters "SWJTU", as demonstrated in Fig. 1**f**, validating the practical application of our bimodal sensor for precise human–machine interactions.

2.2. Microstructure and fundamental characterization

As schematically illustrated in Fig. 2**a**, the discretely patterned ZnO NR arrays were designed to disrupt the lateral transport paths, thereby suppressing the screening effect. The fabrication began with the sputtering of a uniform ZnO seed layer onto an ITO substrate (**Fig. S1**), followed by the growth of ZnO arrays via low-temperature hydrothermal synthesis and photolithography. To further isolate the arrays and prevent electrical leakage, a polyvinylidene fluoride (PVDF) solution was spin-coated onto the patterned ZnO arrays to fill the interstitial spaces. The top-view scanning electron microscopy (SEM) images in Fig. 2**b and 2c** reveal a distinct morphological contrast between the non-patterned and patterned ZnO. The non-patterned sample forms a dense, continuous film, a structure conducive to electron percolation that exacerbates the screening effect. Conversely, the patterned sample exhibits well-isolated, discrete NR arrays. The detailed geometry of the ZnO NR arrays can be found in Table 1 (**Supplementary Information**). This structural difference directly impacts the electrical properties. Under the same bias voltage, the *I-V* curves show a reduction in the output current for the patterned structure, indicating a lower effective carrier density (Fig. 2**d**). This was further quantified by Mott-Schottky analysis (Fig. 2**e**). Both samples exhibit positive slopes, confirming n-type conductivity, however, the calculated carrier concentration decreases from 1.66×10^{19} to 1.26×10^{19} cm^{-3} upon patterning (Fig. 2**f**). This reduction in carrier concentration is pivotal for mitigating the screening effect [40,41]. Furthermore, the X-ray diffraction patterns (Fig. 2**g**) confirm that the patterned ZnO NRs retain a strong (002) diffraction peak, confirming a high degree of c-axis orientation for optimal piezoelectric response. More intriguingly, when mechanical stress is applied along this polar axis, the induced piezopotential can differentially bend the energy bands at opposite ends of the NRs, with the modulation profile being influenced by the patterning geometry (Fig. 2**h**). After confirming that patterning reduces the intrinsic carrier concentration in ZnO, we further investigated its effect on the polarization charge distribution. Finite element simulation results indicate that the patterned structure, with a reduced carrier concentration, sustains significantly higher piezoelectric potential to external forces compared to its non-patterned counterpart under an identical external force (Fig. 2**i-j**). The statistical results in Fig. 2**k** show that the sensitivity of patterned ZnO (0.78 V/MPa) is approximately 1.75 times greater than that of the non-patterned device (0.445 V/MPa). These combined structural, electrical, and simulation results consistently demonstrate that the patterned array design successfully achieves its goal of carrier depletion, leading to enhanced piezopotential and device sensitivity.

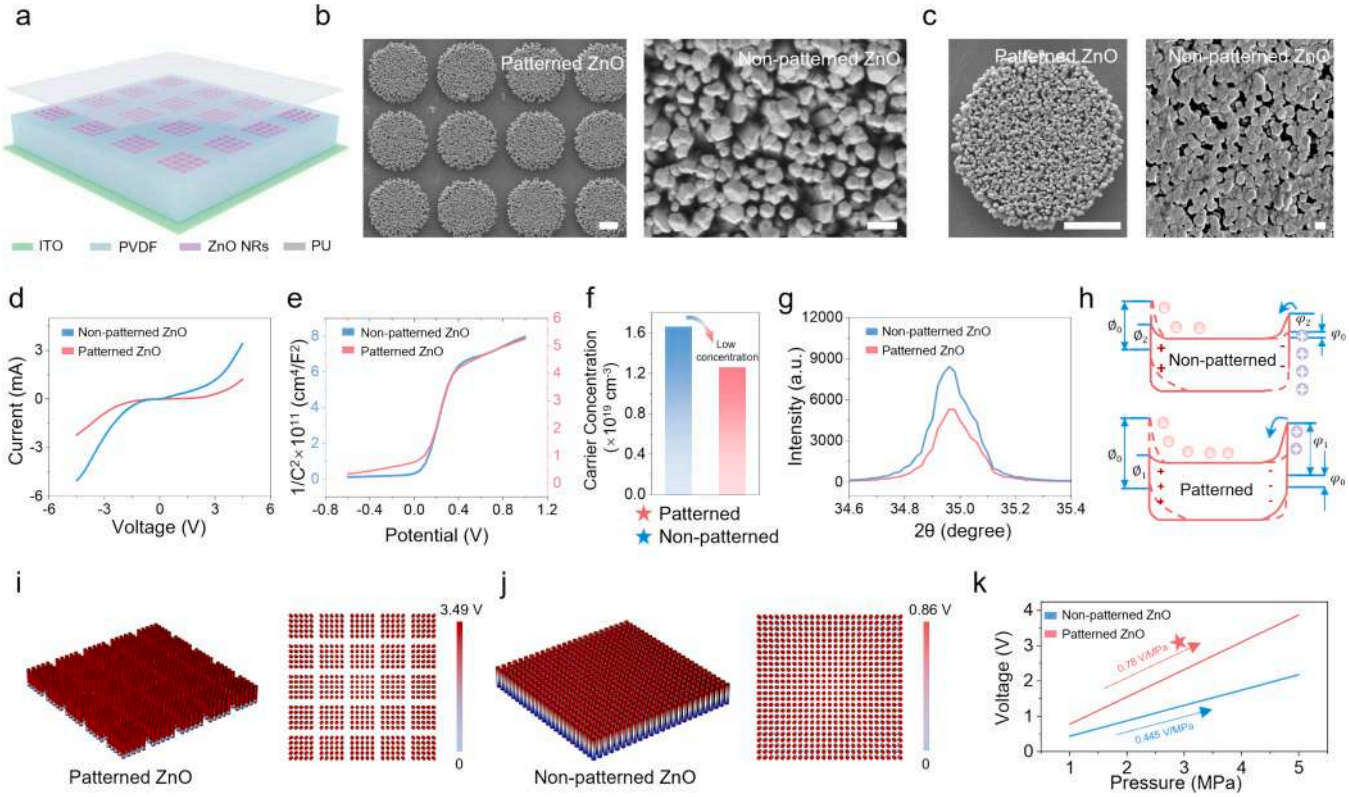


Fig. 2. Microstructure and fundamental characterization of patterned and Non-patterned ZnO. (a) Schematic of macroscopic arrays of patterned ZnO. SEM images of wide-area (b) and single array (c) of patterned (left, scale bars are 5 μm) and non-patterned (right, scale bars are 500 nm) ZnO. (d) *I-V* characteristics of patterned and non-patterned ZnO. Mott-Schottky plots (e) and calculated carrier concentration (f) of the patterned and non-patterned ZnO. XRD patterns (g) and energy band diagrams (h) of patterned and non-patterned ZnO. (i-j) Simulation results of piezoelectric outputs with different patterned structures. (k) Effect of patterned structures on the force-sensitive characteristics of ZnO.

2.3. Electrical performance of PZBD

To investigate the dual-modal sensing capability, the PZBD was encapsulated in a layered stack structure, consisting, from bottom to top, an ITO conductive substrate, patterned ZnO NR arrays, a PVDF insulation layer, and Ag electrodes, as illustrated in Fig. 3**a**. The operational mechanism relies on the piezotronic modulation of the Schottky barrier height at the Ag-ZnO interface (Fig. 3**b**). Under compressive stress along the c-axis of ZnO NR, negative piezopotentials induced at the ZnO surface elevate the Schottky barrier height, thereby impeding electron transport. This synergy of piezoelectric polarization, barrier modulation, and current regulation governs the force-sensitivity of the PZBD. The influence of patterning on piezoelectric polarization charges was examined from both micro- and macro-perspectives. As shown in Fig. 3**c**, piezoresponse force microscopy (PFM) results confirmed a discrete, three-dimensional array morphology with nanorod heights of approximately 1.5 μm. The corresponding surface piezoelectric response mapping indicated intensified responses at the step edges compared to central regions (Fig. 3**d**). This observation aligns with our hypothesis that the array structure effectively suppresses carrier screening, resulting in a localized concentration of piezoelectric polarization charge. Macroscopic measurements confirmed that the patterned ZnO generated nearly twofold the output current of non-patterned films (Fig. 3**e-f**). This enhancement correlates with the observed reduction in carrier concentration, validating that patterning amplifies available polarization charges for high-performance operation. A consistent trend was observed in replicate devices, with patterned structures consistently yielding a twofold increase in current output (**Fig. S2**). Analysis of a single compression-release cycle (**Fig. S3**) revealed the establishment of opposing piezopotentials at the top and bottom ends of ZnO NRs, respectively. As shown in **Fig. S4**, the pressure-dependent *I-V* characteristics of the PZBD indicate that both the forward and reverse currents change dramatically with increasing applied pressure. These current shifts remain consistent across various biases (Fig. 3**g**). Notably, the relative current change ($\Delta I/I_0$) reached 88.1 under a bias of −0.6 V and an applied force of 9 N (Fig. 3**h**). Consequently, the PZBD exhibits a stable, stepped response to static loads ranging from 5 to 25 N with a sensitivity of 6.28 μA/N (Fig. 3**i**). Crucially, while conventional piezoelectric sensors fail to detect static force, the PZBD retains 76.2% of its initial output over 1000 s under a sustained static load of 20 N (Fig. 3**j**). This static sensing capability is attributed to the sustained modulation of the Schottky barrier height by the unscreened piezopotential. A radar chart highlights the advantages of the low-carrier-density design, including higher sensitivity, enhanced piezoelectric output, and robust bimodal sensing capability (Fig. 3**k**).

2.4. Morse code recognition via machine learning based on PZBD

Benefitting from robust electromechanical coupling, the PZBD enables precise monitoring of both dynamic and static forces within a monolithic structure, making it highly suitable for advanced tactile sensing. As a proof-of-concept demonstration, we developed a Morse code decoding system, as outlined in Fig. 4**a**. In this system, mechanical signals captured by the sensor are encoded according to Morse code convention, where transient dynamic impact signals (short duration) are defined as “dot” (binary “1”), while sustained static pressing signals

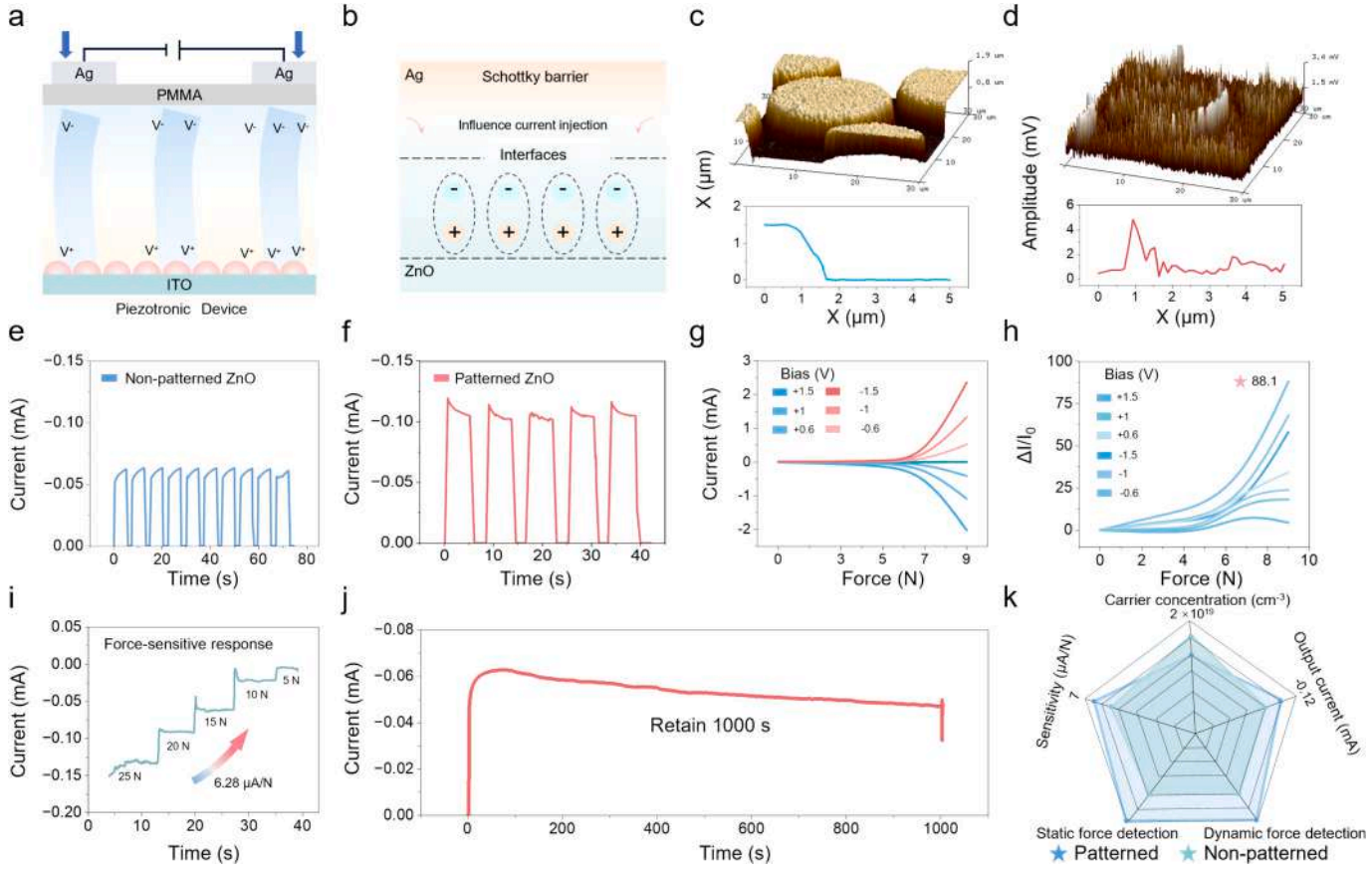


Fig. 3. Electrical characterization of PZBD. Schematic diagram of the structure (a) and micro-working mechanism (b) of the PZBD. PFM testing results of surface topography (c) and potential distribution (d) of patterned ZnO NR arrays. Output currents of the non-patterned (e) and patterned (f) ZnO. (g) Current versus pressure in the PZBD under biases of − 1.5, −1, −0.6, 0, 0.6, 1 and 1.5 V. (h) Current change ratio ($\Delta I/I_0$) versus pressure for the PZBD under various forward and reverse biases. (i) Relative change in the current of the PZBD under gradient static forces of 5 ~ 25 N. (j) *I-t* curve of the PZBD under a force of 20 N over 1000 s. (k) Radar chart for comparing the different performances of the two sensors.

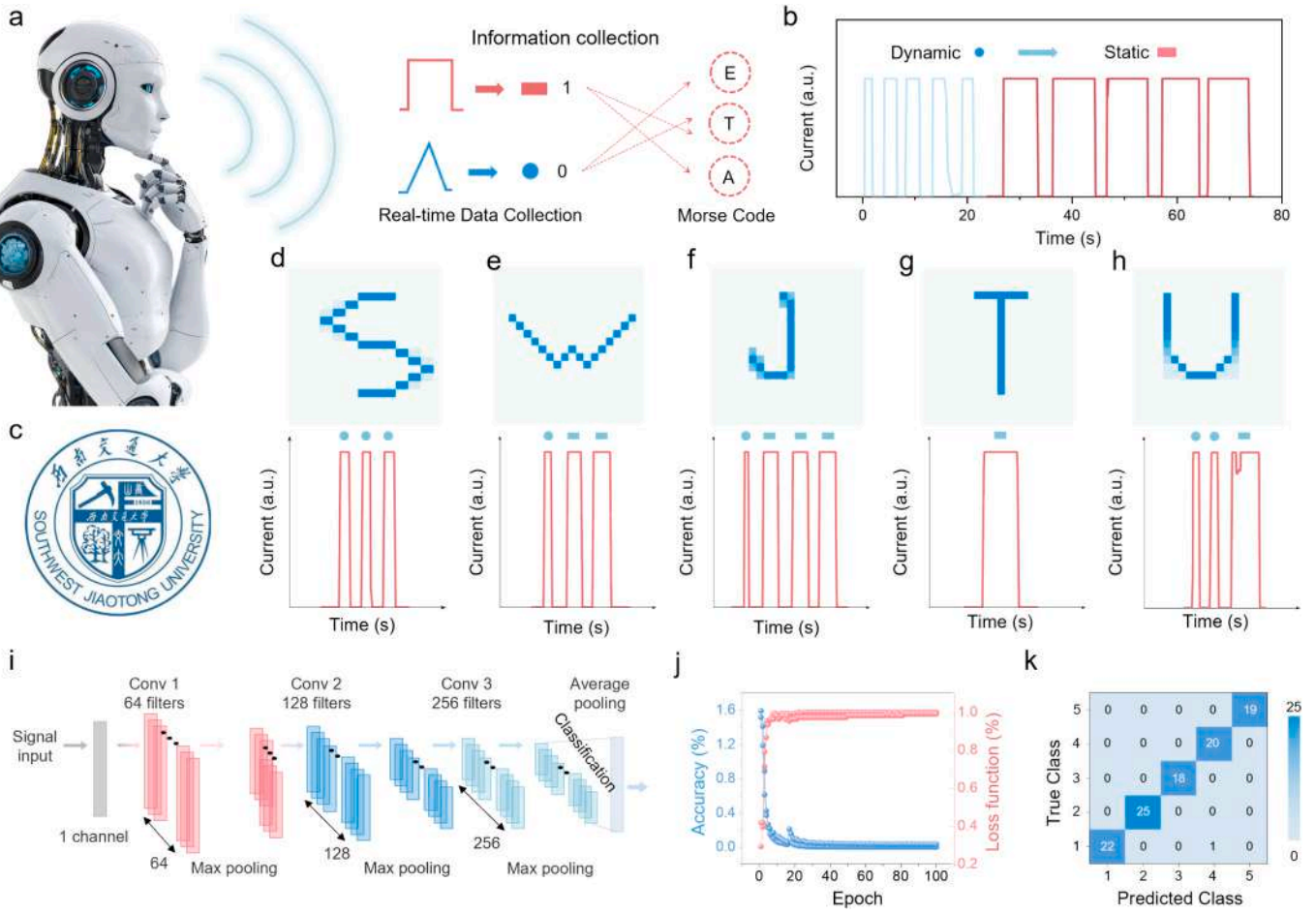


Fig. 4. Morse code decoding system based on PZBD assisted with machine learning. (a) Schematic diagram of Morse code identification via PZBD. Through permutations and combinations, different letters can be identified. Application demonstration using the letters "SWJTU". (b) Current of the PZBD under dynamic and static forces. Transient dynamic impact signals (short duration) are set to 0, and the sustained static pressing signals (long duration) are set to 1. (c) Target object for identification. (d-h) Recognition results for 5 letters and their corresponding current responses. (i) Detailed architecture of the constructed 1D-CNN model. (j) Classification accuracy and loss function of the training and validation datasets in 100 epochs. (k) Confusion matrix for the recognition of 5 letters.

(long duration) represent "dash" (binary "0"). These binary sequences are subsequently mapped to alphanumeric characters through predefined combinations. As illustrated in Fig. 4**b**, dynamic stimuli (blue curve) generate sharp, periodic current pulses, whereas static stimuli (red curve) yield continuous and stable current plateaus. This pronounced temporal and waveform disparity offers robust criteria for subsequent signal classification. Next, we validated the system by encoding the letter sequence "SWJTU" (Fig. 4**c**). The corresponding current responses and mapping results for the five Morse code characters are shown in Fig. 4**d-h**. The current response curve for each character precisely matches the corresponding Morse code in terms of pulse count, duration, and waveform characteristics. For example, the character "T" (a single dash) corresponds to a single, wide current peak, while the character "U" (dot-dot-dash) is represented by two narrow peaks and one wide peak. The continuous, sequential recognition of these five letters is demonstrated in **Fig. S5**, validating reliable signal conversion across both dynamic and static force modalities. Following data acquisition, the current response features were digitally extracted and fed into a convolutional neural network (CNN) algorithm for multilayer analysis and classification (Fig. 4**i**). The training process exhibited rapid convergence, indicating efficient feature learning from the signal waveforms (Fig. 4**j**). The confusion matrix reveals a recognition accuracy of 99% for the test set (Fig. 4**k**). The successful demonstration of Morse code recognition confirms that this bimodal sensor is capable of distinguishing between transient dynamic stimuli and sustained static forces. By integrating bimodal sensing into a single device, this approach eliminates the need for complex signal decoupling in hybrid structures, offering distinct advantages for miniaturized, low-cost intelligent systems. As such, the developed device holds significant potential for advancing HMI systems, such as identity recognition, remote sensing, and authentication, paving the way for more intuitive and intelligent interactive technologies.

3. Conclusion

In summary, we developed a bimodal piezotronic sensor based on photolithographically patterned ZnO nanorod arrays. The discrete array architecture effectively reduces the carrier concentration, thereby suppressing the piezoelectric screening effect and yielding a twofold enhancement in the piezoelectric output compared to non-patterned films. Leveraging this enhanced piezotronic effect, the fabricated sensor achieves dual-mode force detection, exhibiting a high sensitivity to dynamic stimuli while maintaining a stable response to static loads for over 1000 s. Furthermore, when integrated with a machine-learning-assisted system, the developed sensor demonstrated accurate Morse code recognition with an accuracy of 99%. This study not only provides deep insights into the interface engineering of piezotronic devices but also demonstrates a viable pathway for advanced tactile perception in intelligent systems.

4. Experimental section

4.1. Fabrication of PZBD

Patterned and non-patterned ZnO thin films were fabricated via a low-temperature hydrothermal method. First, conductive glass substrates (ITO, 20 mm × 20 mm) were ultrasonically cleaned sequentially with acetone, ethanol, and deionized water, then dried with nitrogen gas. Subsequently, a ZnO seed layer was deposited on the conductive glass surface by radio frequency (RF) magnetron sputtering for 1.5 h. During sputtering, the flow rate ratio of argon to oxygen was set to 40:1, and the sputtering power was 60 W. To prepare the growth solution, 0.1 M zinc nitrate hexahydrate ($Zn(NO_3)_2{\cdot}6H_2O$) and 0.1 M hexamethylenetetramine ($C_6H_{12}N_4$) were mixed in a blue-necked bottle. Afterwards, the glass substrates coated with the seed layer were immersed in the growth solution and placed in an oven at 80 °C for 5 h under constant temperature. Later, polyvinylidene fluoride (PVDF) was used as a barrier layer and uniformly coated onto the surfaces of the ZnO thin films. The spin-coating process parameters were set as follows: First, spin-coating was performed at 500 rpm for 10 s, and then spin-coating was performed at 3000 rpm for 30 s. After that, the films were baked at 80 °C for 1 h. To construct a planar electrode structure, Ag electrodes (2 mm × 2 mm) were deposited on the ZnO thin films by RF magnetron sputtering. Silver paste was used to clamp and connect the electrodes with copper wires to optimize the interface performance. Finally, the device was encapsulated with a commercial polyurethane (PU) film for subsequent testing.

4.2. Characterizations

The morphology of ZnO thin films was characterized by SEM (JSM-7800F). X-ray diffraction (XRD, DX-1000 diffractometer) was used to determine the crystal structure of the samples. For electromechanical measurements, the pressure was applied using a linear motor (LinMot *H*01–23 × 86/160) mounted with a digital force gauge (M7–50, Mark-10). The *I–V* characteristics were measured using a Keithley 2700 test system with a sweeping voltage between − 3 and + 3 V. During the periodic *I-t* characteristic test, the applied voltage was −0.6 V. The electrical properties of the samples were recorded using a Keithley 6514 system. Mott-Schottky plots were obtained from the CHI660E electrochemical station. A UV2310II dual beam UV–visible spectrophotometer was used to measure the absorption spectrum. The surface piezoelectric response images of ZnO thin films were investigated by an atomic force microscope (AFM, Bruker Corporation) in piezoresponse force microscopy (PFM) mode.

4.3. Finite element simulation

All simulations were performed using COMSOL Multiphysics with the Piezoelectric Devices module. A stationary solver with a convergence criterion of 1×10^{-7} was employed, and quadratic elements were used for both the mechanical and electrical fields. Local mesh refinement was applied in critical regions to ensure numerical accuracy. For mechanical boundary conditions, the bottom surface of the ZnO was fixed, while the top surface was either free or subjected to uniaxial compression depending on the simulation scenario. Lateral surfaces were constrained in the transverse direction to avoid spurious deformation. Electrical boundary conditions included grounding of the bottom electrode and a floating potential on the top electrode.

4.4. Deep learning for Morse code recognition

The CNN models were developed in Python based on TensorFlow and Keras frameworks. The 1D-CNN model was developed for data feature extraction and Morse code recognition. The length of each data entry into the 1D-CNN analytics was 100. We first trained the model with 80% of the data, then calibrated the model with 10% of the data, and finally used the remaining 10% to test the corrected optimal model parameters. A stochastic gradient descent algorithm was used to train the CNN model. The classification accuracy and loss function were evaluated to test the deep learning effect by adjusting the parameters. With the assistance of the 1D-CNN algorithm, 100 training periods could achieve Morse code recognition.

Declaration of competing interest

The authors declare that they have no known competing financial interests or personal relationships that could have appeared to influence the work reported in this paper.

Acknowledgements

This project is supported by Beijing Key Laboratory of High-Entropy Energy Materials and Devices, Beijing Institute of Nanoenergy and Nanosystems (No.GS2025MS021). This research was financially supported by the National Natural Science Foundation of China (No. U2330120) and the Basic Research Cultivation Project of Southwest Jiaotong University (No. 2682023KJ024). Thanks for the help from the Analysis and Testing Center of Southwest Jiaotong University.

Appendix A. Supplementary data

Supplementary data to this article can be found online at https://doi.org/10.1016/j.cossms.2026.101273.

Data availability

Data will be made available on request.

References

[1] W. Wang, Y. Jiang, D. Zhong, et al., Neuromorphic sensorimotor loop embodied by monolithically integrated, low-voltage, soft e-skin, Science 380 (2023) 735–742.
[2] H. Xu, W. Zheng, Y. Zhang, et al., A fully integrated, standalone stretchable device platform with in-sensor adaptive machine learning for rehabilitation, Nat. Commun. 14 (2023) 7769.
[3] M. Chen, J. Liu, Y. Hu, et al., Silk fibroin-based flexible pressure sensors: processing and application, Mater. Futures 3 (3) (2024) 032501.
[4] W. Deng, Y. Zhou, A. Libanori, et al., Piezoelectric nanogenerators for personalized healthcare, Chem. Soc. Rev. 51 (2022) 3380–3435.
[5] N. Zhang, Y. He, L. Wang, Designing iontronic pressure sensors: a perspective from multiscale mechanics, Iontronics 1 (2025) 5.
[6] Z. Yao, W. Wu, F. Gao, et al., Flexible tactile sensing systems: challenges in theoretical research transferring to practical applications, Nano-Micro Lett. 18 (2026) 37.
[7] X. Wang, C. Guo, Z. Su, et al., Flexible iontronic pressure sensing technology: advanced structural ionic layer, Iontronics 2 (2026) 1.
[8] M. Deng, Z. Ren, J. Yin, et al., A constructive perspective on ionic self-powered pressure sensing, Prog. Mater Sci. 157 (2026) 101595.
[9] Y. Sun, G. Tian, W. Deng, et al., Ionic hydrogel sensors toward next-gen personalized healthcare, Adv. Mater. 38 (2026) e09122.
[10] Y. Dai, H. Hu, M. Wang, et al., Stretchable transistors and functional circuits for human-integrated electronics, Nat. Electron. 4 (1) (2021) 17–29.
[11] X. Li, Y. Sun, S. Wang, et al., Body temperature-triggered adhesive ionic conductive hydrogels for bioelectrical signal monitoring, Chem. Eng. J. 498 (2024) 155195.
[12] B. Zhou, J. Liu, X. Huang, et al., Mechanoluminescent-triboelectric bimodal sensors for self-powered sensing and intelligent control, Nano-Micro Lett. 15 (2023) 72.
[13] G. Tian, W. Deng, T. Yang, et al., Hierarchical piezoelectric composites for non-invasive continuous cardiovascular monitoring, Adv. Mater. 36 (2024) 2313612.
[14] S. Feng, J. Li, L. Feng, et al., Dual-mode conversion of photodetector and neuromorphic vision sensor via bias voltage regulation on a single device, Adv. Mater. 35 (2023) 2308090.
[15] T. Wang, T. Jin, W. Lin, et al., Multimodal sensors enabled autonomous soft robotic system with self-adaptive manipulation, ACS Nano 18 (2024) 9980–9996.
[16] F. Kao, H. Ho, P.Y. Chiu, et al., Self-assisted wound healing using piezoelectric and triboelectric nanogenerators, Sci. Technol. Adv. Mater. 23 (2022) 1–16.
[17] H. Niu, H. Li, S. Gao, et al., Perception-to-cognition tactile sensing based on artificial-intelligence-motivated human full-skin bionic electronic skin, Adv. Mater. 34 (2022) 2202622.

[18] X. Xu, B. Yan, Bioinspired luminescent HOF-based foam as ultrafast and ultrasensitive pressure and acoustic bimodal sensor for human-machine interactive object and information recognition, Adv. Mater. 35 (2023) 2303410.
[19] R. Ge, Q. Yu, F. Zhou, et al., Dual-modal piezotronic transistor for highly sensitive vertical force sensing and lateral strain sensing, Nat. Commun. 14 (2023) 6315.
[20] Q. Yu, R. Ge, J. Wen, et al., Highly sensitive strain sensors based on piezotronic tunneling junction, Nat. Commun. 13 (2022) 778.
[21] Y. Chen, G. Gao, J. Zhao, et al., Piezotronic graphene artificial sensory synapse, Adv. Funct. Mater. 29 (2019) 1900959.
[22] Y. Zhang, J. Chen, R. Yu, et al., High-performance piezotronic devices, ACS Nano ,19(7) (2025) 6705–6728.
[23] Y. Wang, Q. Sun, Z. Wang, Piezotronics and tribotronics of 2D materials, Mater. Sci. Eng. R 164 (2025) 100951.
[24] F. Pang, P. Zhao, H.Y. Lee, et al., Progress and perspectives in 2D piezoelectric materials for piezotronics and piezo-phototronics, Adv. Sci. 12 (2025) 2411422.
[25] C. Pan, J. Zhai, Z.L. Wang, Piezotronics and piezo-phototronics of third generation semiconductor nanowires, Chem. Rev. 119 (2019) 9303–9359.
[26] L. Wang, Z. Wang, Advances in piezotronic transistors and piezotronics, Nano Today 37 (2021) 101108.
[27] X. Wang, X. He, H. Zhu, et al., Subatomic deformation driven by vertical piezoelectricity from CdS ultrathin films, Sci. Adv. 2 (2016) e1600209.
[28] C. An, H. Qi, L. Wang, et al., Piezotronic and piezo-phototronic effects of atomically-thin ZnO nanosheets, Nano Energy 82 (2021) 105653.
[29] S. Liu, L. Wang, Z. Wang, et al., Double-channel piezotronic sensor for highly sensitive pressure sensing, ACS Nano 12 (2018) 1732–1738.
[30] W. Wu, X. Wen, Z. Wang, Taxel-addressable matrix of vertical-nanowire piezotronic transistors for active and adaptive tactile imaging, Science 340 (2013) 952–957.
[31] J. Zhou, Y. Gu, P. Fei, et al., Flexible piezotronic strain sensor, Nano Lett. 8 (2008) 3035–3040.
[32] L. Wang, S. Liu, Z. Wang, et al., Piezotronic effect enhanced photocatalysis in strained anisotropic ZnO/TiO2 nanoplatelets via thermal stress, ACS Nano 10 (2016) 2636–2643.
[33] W. Wu, Y. Wei, Z.L. Wang, Strain-gated piezotronic logic nanodevices, Adv. Mater. 22 (2010) 4711.
[34] Z. Wang, Piezopotential gated nanowire devices: piezotronics and piezo-phototronics, Nano Today 5 (6) (2010) 540–552.
[35] Z. Wang, J. Song, Piezoelectric nanogenerators based on zinc oxide nanowire arrays, Science 312 (5771) (2006) 242–246.
[36] J. Zhao, Z. Wei, Q. Zhang, et al., Static and dynamic piezopotential modulation in piezo-electret gated MoS2 field-effect transistor, ACS Nano 13 (1) (2019) 582–590.
[37] Z. Wang, Y. Sun, S.L. Wang, et al., Insight into piezoelectricity modulation mechanism of ZnO doped with Y ions, J. Mater. Chem. A 12 (2024) 12435–12442.
[38] V.R. Lebaka, P. Ravi, M.C. Reddy, et al., Zinc oxide nanoparticles in modern science and technology: Multifunctional roles in healthcare, environmental remediation, and industry, Nanomaterials 15 (2025) 754.
[39] L. Wang, S. Liu, X. Feng, et al., Ultrasensitive vertical piezotronic transistor based on ZnO twin nanoplatelet, ACS Nano 11 (2017) 4859–4865.
[40] Y. Sun, S. Shen, W. Deng, et al., Suppressing piezoelectric screening effect at atomic scale for enhanced piezoelectricity, Nano Energy 105 (2023) 108024.
[41] G. Tian, D. Xiong, Y. Su, et al., Understanding the potential screening effect through the discretely structured ZnO nanorods piezo array, Nano Lett. 20 (2020) 4270–4277.
[42] C. Wang, K. Lai, Y. Li, et al., Ultrasensitive thin-film-based AlxGa1-xN piezotronic strain sensors via alloying-enhanced piezoelectric potential, Adv. Mater. 27 (2015) 6289–6295.
[43] Y. Su, K. Gupta, Y.L. Hsiao, et al., Gigantic enhancement of electricity generation in piezoelectric semiconductors by creating pores as a universal approach, Energ. Environ. Sci. 12 (2019) 410–417.
[44] J. Villafuerte, X. Zhang, E. Sarigiannidou, et al., Boosting the piezoelectric coefficients of flexible dynamic strain sensors made of chemically-deposited ZnO nanowires using compensatory Sb doping, Nano Energy 114 (2023) 108599.
[45] S. Liu, L. Wang, Z. Wang, et al., Double-channel piezotronic transistors for highly sensitive pressure sensing, ACS Nano 12 (2018) 1732–1738.
[46] P. Pandit, M. Chougale, D. Dubal, et al., Amplifying touch using 3D ZnO tetrapods for tactile and haptic intelligence, Small 21 (2025) 2408414.
[47] P. Inphak, P. Kaewdee, C. Randorn, et al., Multifunctional PAM/ZnO PolyHIPE hydrogel composite beads for air purification: Synergistic particulate matter filtration and photocatalytic remediation of airborne PAHs, Appl. Catal. B 381 (2026) 125825.
[48] Z. Pan, W. Peng, F. Li, et al., Carrier concentration-dependent piezotronic and piezo-phototronic effects in ZnO thin-film transistor, Nano Energy 49 (2018) 529–537.
[49] Z. Wang, S. Wang, B. Lan, et al., Piezotronic sensor for bimodal monitoring of Achilles tendon behavior, Nano-Micro Lett. 17 (2025) 241.
[50] W. Deng, Z. Wang, H. Zhang, et al., Surface engineered ZnO nanorods array for multidirectional force detection, J. Alloy. Compd. 1020 (2025) 179397.
[51] Z.L. Wang, W. Wu, Recent advances in piezotronics and piezo-phototronics, MRS Bull. 50 (2025) 115–122.